Available online at www.sciencedirect.com
SCIENCE DIRECT
Journal of Catalysis 231 (2005) 213–222
JOURNAL OF CATALYSIS
www.elsevier.com/locate/jcat

Photocatalytic water splitting over iron oxide nanoparticles intercalated in $HTiNb(Ta)O_5$ layered compounds

Jum Suk Jang, Hyun Gyu Kim, Vangala R. Reddy, Sang Won Bae, Sang Min Ji, Jae Sung Lee *

Department of Chemical Engineering and School of Environmental Engineering, Pohang University of Science and Technology (POSTECH), San 31 Hyoja-dong, Pohang 790-784, Republic of Korea

Received 23 October 2004; revised 26 December 2004; accepted 18 January 2005

Abstract

Nanosized iron oxide particles were intercalated into the interlayer of layered compounds $HTiNb(Ta)O_5$ by a successive ion-exchange reaction. The electronic and local coordination structures of iron oxide in the interlayer space of these proton-containing compounds were investigated by X-ray absorption near edge structure (XANES) and X-ray photoelectron spectroscopy (XPS). The intercalated nanosized iron oxide was Fe_2O_3, which exhibited a high electron deficiency. Unlike in a previous report, Fe_2O_3-intercalated layered compounds did not produce hydrogen from an aqueous methanol solution in a photocatalytic manner under visible light. Instead, the material produced a stoichiometric mixture of hydrogen and oxygen photocatalytically under UV irradiation and produced oxygen from an aqueous $AgNO_3$ solution photocatalytically under visible light.

Keywords: Layered compounds; Iron oxide nanoparticles; H_2 evolution; Photocatalysts

1. Introduction

Sunlight is a clean, renewable, and abundant energy source, and its conversion to hydrogen has been considered an ideal way to counter the depletion and environmental problems of fossil fuels. Of the various proposed methods, photocatalytic water splitting (PWS) with the use of solar energy is an attractive route for energy conversion because it converts water directly into hydrogen, the critical energy carrier of the future. Since its first demonstration in 1972 by Honda and Fujishima [1], PWS has developed steadily into an efficient process, at least under UV-light irradiation. Current state-of-the-art photocatalysts split water into hydrogen and oxygen gases under UV light with quantum yields (the fraction of absorbed photon used for hydrogen production) as high as 50% [2,3]. However, UV light accounts for only ca. 4% of the solar energy spectrum, and visible light occupies 46% of the spectrum. The development of visible light-active photocatalysts, therefore, has become one of the most important topics in photocatalysis research today.

There are many common strategies for developing photocatalysts, which are photoactive under visible light [4–10]. Among them, the intercalation of a visible light-active photocatalyst into a host material with a large band gap is a promising method for decomposing water under visible light irradiation [11,12]. In a series of publications, Sato and co-workers [12–14] have reported the intercalation of nanosized Fe_2O_3, TiO_2, and CdS particles into the interlayer of layered compounds such as $HNbWO_6$ or $HTaWO_6$. Their photoactivity was improved markedly over those of unintercalated photocatalyst particles, which was ascribed to an effective separation of photogenerated electrons and holes due to their rapid diffusion. Of particular interest in these intercalated nanoparticles was the production of hydrogen from water containing a sacrificial agent (CH_3OH) under visible light irradiation with quantum yields as high as 10% [12].

We have been interested in these systems of intercalated nanoparticles as effective means of combining two photo-

* Corresponding author. Fax: 82-562-279-5799.
E-mail address: jlee@postech.ac.kr (J.S. Lee).

0021-9517/$ – see front matter
doi:10.1016/j.jcat.2005.01.026

catalytic functions and taking advantage of their synergistic effects. However, we were also puzzled by the photocatalytic hydrogen production from water over Fe_2O_3-containing layered compounds, since bulk Fe_2O_3 could not produce hydrogen from water because the bottom of its conduction band is located at a less negative position than the reduction potential of water to hydrogen. Therefore, photoelectrons formed in the conduction band of Fe_2O_3 would not have enough potential to reduce water unless the iron species formed in the interlayer space has an electronic structure completely different from that of the bulk. Fe_2O_3 nanoparticles, have been extensively studied in their own right because of their applications in magnetic storage, gas sensing, and chemical catalysis [15–17]. Thus, in this work, we intercalated iron oxide nanoparticles into two layered compounds, $HTiNbO_5$ and $HTiTaO_5$. Then the electronic and local coordination structures of iron oxide intercalated into the interlayer space of these proton-containing layered compounds were investigated by X-ray absorption near edge structure (XANES) and X-ray photoelectron spectroscopy (XPS). Then the composite photocatalysts of Fe_2O_3 nanoparticles intercalated into the interlayer were evaluated for their catalytic performance in overall water splitting under UV and hydrogen production from a water–methanol mixture under visible-light irradiation.

2. Experimental

2.1. Preparation of host materials

$KTi(Nb)TaO_5$ was prepared by a solid-state reaction of K_2CO_3, TiO_2, and Ta_2O_5 (or Nb_2O_5) supplied by Aldrich (99.9% purity). An excess amount of K_2CO_3 (20 mol%) was added to compensate for the loss due to the volatilization of the potassium. The mixtures were well ground by a ball mill with the wet grinding method in ethanol. The ground mixtures were pressed into pellets under a pressure of 40 MPa. The pellets were calcined in an alumina crucible at 1373 K for 24 h, with intermediate grinding during calcination. The calcined sample was washed with distilled water to remove the excess carbonate. Then we converted the prepared K-forms into proton derivatives by refluxing the solids in 4 M HNO_3 at room temperature for 2 days under continuous stirring with the replacement of acid every 12 h.

2.2. Intercalation of Fe_2O_3 into the interlayer of $HTiNb(Ta)O_5$

The intercalation of iron oxide into the interlayer was achieved by stepwise intercalation reactions. First the interlayer of $HTiNb(Ta)O_5$ was expanded by the intercalation of bulky *n*-propylammonium cations (n-$C_3H_7NH_3^+$). The interlayer protons were replaced now by *n*-propylammonium cations (n-$C_3H_7NH_3^+$) to expand the layers and to facilitate the subsequent pillaring reaction of Fe cations. Alkylammonium intercalation was carried out by the reaction of 1 g of the proton derivative of the layered compounds with *n*-propylamine (5 ml) in heptane solution (10 ml) at 48 °C for 3 days. The reaction products were separated by centrifugation, washed with distilled water several times, and dried at 100 °C for 4 h. For the intercalation of Fe_2O_3, its precursor $[Fe_3(CH_3COO)_7(OH)(H_2O)_2]^+$ was prepared as follows: $Fe(NO_3)_3 \cdot 9H_2O$ (40.4 g) (Aldrich; 99.99%) was added to 25 ml of ethyl alcohol (J.T. Baker; 99.99%), and then the solution was reacted with 70 ml of acetic anhydride (Aldrich; 99.99%) that was added in small portions. The resulting precipitate was separated by filtration and used as a precursor without washing. The Fe_2O_3 pillar was constructed in the interlayer space of $HTiNb(Ta)O_5$ pre-swelled with *n*-propylammonium molecules. Thus the pre-swelled layered compound (1 g) was reacted with $[Fe_3(CH_3COO)_7(OH)(H_2O)_2]^+$ (20 g) at 50 °C for 72 h in an aqueous solution. The reaction products were separated by centrifugation, washed with distilled water several times, and dried at 100 °C for 4 h. The iron acetate-hydroxo cation intercalated in the interlayer of layered compounds was converted into iron oxide by calcination at 300 °C for 4 h.

2.3. Characterization

The crystalline phases of the products were determined by powder X-ray diffraction (XRD) (Mac Science Co.; M18XHF) with monochromatic Cu-K_α radiation at 40 kV and 200 mA. The optical properties were analyzed with a UV–visible diffuse reflectance spectrometer (UV-DR Shimadzu; UV 2401). The morphology of these compounds was determined by field emission scanning electron microscopy (SEM) (Hitachi; S-4200), and the BET surface area was evaluated by N_2 adsorption at 77 K in a constant-volume adsorption apparatus (Micrometrics; ASAP 2012). Thermogravimetric analysis (TGA) (Perkin–Elmer) was carried out at a heating rate of 10 °C/min from 40 to 800 °C.

X-ray absorption spectra (XAS) of the Fe K-edge were recorded at the Pohang Accelerator Laboratory (PAL) on beamline BL3C1 operating at 2.5 GeV with ca. 100–160 mA of the stored current. The radiation was monochromatized with the use of a Si(111) double-crystal monochromator to collect high-resolution XAS spectra. Data were collected at room temperature in transmission mode. The intensities of incident and transmitted beams were measured by ionization detectors containing N_2. We calibrated the absorption energy by measuring the X-ray absorption spectrum of Fe metal foil and assigning the first inflection point in the absorbance–energy curve to 7112 eV. The X-ray absorption near edge structure (XANES) analysis was processed according to the following procedure with the program WinXAS 97 (Version 2.3). We normalized the spectra in absorbance by fitting the spectral region with the use of a first-order polynomial function and subtracting this as background absorption. The ionic state of Fe intercalated in the interlayer of layered

compounds was obtained from X-ray photoelectron spectroscopy (XPS) measurements (VG Scientific; ESCALAB 220iXL) with Mg-K_α radiation (1253.6 eV). The binding energy calibration was performed with C 1s peak as the reference energy.

2.4. Photocatalytic reaction procedures

Photocatalytic water splitting under UV irradiation was carried out in a closed gas circulation system at room temperature. The catalyst (0.3 g) was dispersed in distilled water (500 ml) by magnetic stirring and irradiated with a high-pressure mercury lamp (Oriel; 450 W) equipped with an inner irradiation-type quartz cell in the presence of gaseous Ar at 50 Torr. The same reaction under visible irradiation was performed in an outer-irradiation-type Pyrex reactor with a similar mercury lamp (Oriel; 500 W). The UV part of irradiations was removed with a cutoff filter ($\lambda > 420$ nm). The catalyst (0.1 g) was suspended by magnetic stirring in distilled water containing methanol as a hole scavenger or $AgNO_3$ as an electron acceptor (80 ml of H_2O + 20 ml of methanol or 0.01 M $AgNO_3$, 100 ml aqueous solution). The rates of evolution of H_2 and O_2 were determined from analysis of gas products by gas chromatography (TCD, molecular sieve 5-Å column, Ar carrier).

3. Results and discussion

3.1. Physical characterization

The TGA curves of the iron precursor intercalated in $HTiNb(Ta)O_5$ were measured in air flow and in a temperature range of 40–800 °C as shown in Fig. 1. The initial weight loss from 40 to 150 °C can be attributed to the dehydration of the interlayer water or the dehydroxylation of partially hydrolyzed iron hydroxides. The drastic weight loss from 150 to 300 °C was due to the oxidative decomposition of acetyl groups of the interlayer complex. The further weight loss at higher temperatures was ascribed to the decomposition of intermediate organic residues and to the loss of iron from the interlayer. It was generally observed that iron intercalated into the interlayer of $HTiNbO_5$ showed more weight loss than that of $HTiTaO_5$.

Fig. 2A shows X-ray diffraction (XRD) patterns of (a) $HTiNbO_5$, (b) $HTiNbO_5$/*n*-$C_3H_7NH_2$, (c) $HTiNbO_5$/Fe-100 °C, and (d) $HTiNbO_5$/Fe-300 °C, where temperatures denote the temperatures of calcination after intercalation of the iron precursor. After intercalation of *n*-$C_3H_7NH_2$ and iron into the interlayer of layered compounds, all of the catalysts showed a (002) diffraction peak as that of the host lattice ($HTiNbO_5$), indicating that the layered structure was retained. But (002) peaks of intercalated materials were shifted to smaller angles because of expansion of the interlayer of layered compounds by incorporation of *n*-$C_3H_7NH_2$ and iron. The (002) diffraction peak of $HTiNbO_5$/*n*-$C_3H_7NH_2$ shifted to the largest extent toward a lower 2θ angle, which indicated that the expansion of the layers was larger for *n*-$C_3H_7NH_2$ than for the other samples. The $HTiNbO_5$/Fe-100 °C dried at 100 °C for 4 h contained $[Fe_3(CH_3COO)_7(OH)(H_2O)_2]^+$ complex cations in interlayers of the layered compound, whereas $HTiNbO_5$/Fe-300 °C had been calcined at 300 °C for 4 h to obtain an iron oxide in the interlayer of the layered compound. Successful intercalation of the oxides was observed by the shift in the 2θ angle. Two small peaks were observed, corresponding to (111) and (200) planes of Fe_2O_3, as indicated by vertical lines in Fig. 2. The $HTiNbO_5$/Fe-300 °C sample clearly

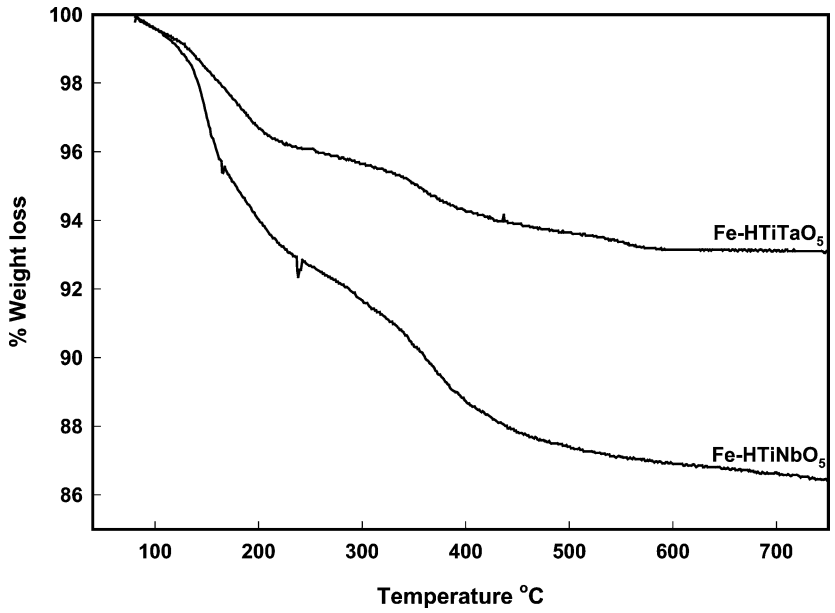

Fig. 1. TGA curve of $HTiNbO_5$/Fe-precursor, $HTiTaO_5$/Fe-precursor.

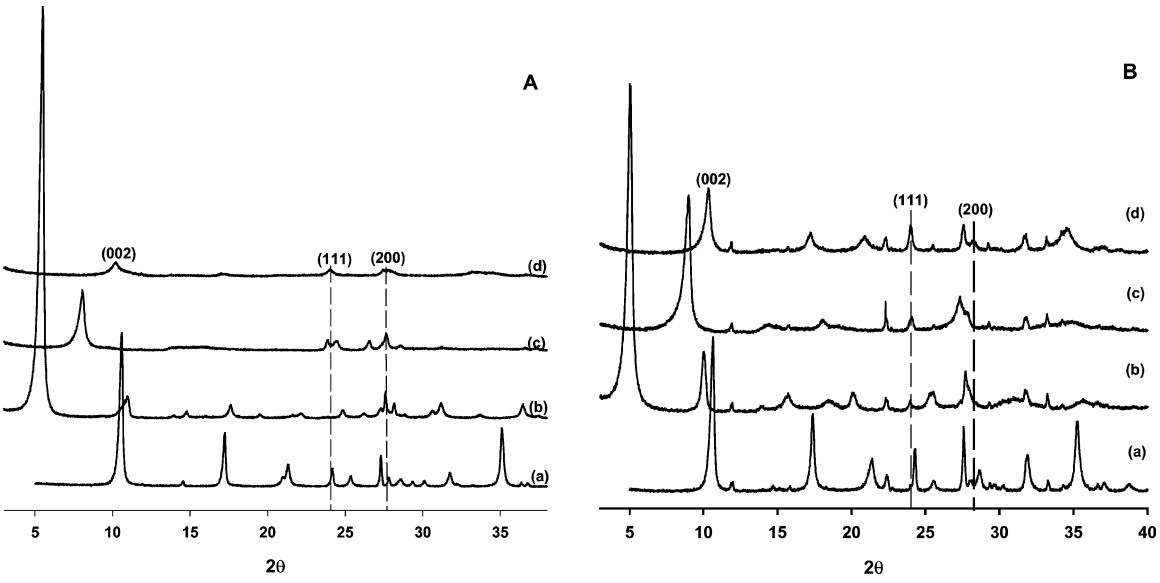

Fig. 2. A: XRD patterns of (a) $HTiNbO_5$, (b) $HTiNbO_5$/*n*-$C_3H_7NH_2$, (c) $HTiNbO_5$/Fe-100 °C, (d) $HTiNbO_5$/Fe-300 °C. B: XRD patterns of (a) $HTiTaO_5$, (b) $HTiTaO_5$/*n*-$C_3H_7NH_2$, (c) $HTiTaO_5$/Fe-100 °C, (d) $HTiTaO_5$/Fe-300 °C. Two vertical lines indicate the expected positions of (111), (200) peaks of Fe_2O_3.

Table 1
Band-gap energies (E_g), interlayer lattic distances and surface areas for intercalated layered compounds

Host material	Samples	E_g (eV)	2θ of (200)	Interlayer lattic distance (Å)	Surface area (m^2/g)
$HTiNbO_5$	$KTiNbO_5$	3.2	9.58	9.224	3
	$HTiNbO_5$	3.2	10.56	8.370	3
	Propyl-$HTiNbO_5$	3.3	5.46	16.173	5.6
	Fe–$HTiNbO_5$[a]	2.0	8.06	10.960	12
$HTiTaO_5$	$KTiTaO_5$	3.1	9.60	9.206	4.2
	$HTiTaO_5$	3.1	10.58	8.355	4.0
	Propyl-$HTiTaO_5$	3.3	5.04	17.519	6
	Fe–$HTiTaO_5$[a]	2.0	8.96	9.861	14

[a] Calcined at 300 °C.

showed (111) and (200) peaks for Fe_2O_3, but diffraction peaks due to host $HTiNbO_5$ were greatly reduced in intensity. The XRD patterns of $HTiTaO_5$, $HTiTaO_5$/*n*-$C_3H_7NH_2$, $HTiTaO_5$/Fe_2O_3-100 °C, and $HTiTaO_5$/Fe_2O_3-300 °C are qualitatively similar to those of $HTiNbO_5$, as shown in Fig. 2B. But iron-containing samples (Fig. 2c–d) showed more intense (002) peaks compared with $HTiNbO_5$ counterparts. Other peaks due to layered structure material were more intense for tantalate. These indicate that tantalate-based composite material had a more stable structure, as also suggested by TGA results in Fig. 1. The XRD peaks due to Fe_2O_3 were also more intense for tantalate. The 2θ angles of the (002) diffraction peaks and corresponding interlayer spacing are summarized in Table 1.

Fig. 3A shows the UV-diffuse reflection (UV-DR) spectra of (a) $HTiNbO_5$, (b) $HTiNbO_5$/$C_3H_7NH_2$, (c) $HTiNbO_5$/Fe-100 °C, and (d) $HTiNbO_5$/Fe-300 °C. The absorption spectra of $HTiNbO_5$ varied according to the intercalated species present in the interlayer of the layered compound. $HTiNbO_5$/*n*-$C_3H_7NH_2$ shows the absorption edge, slightly blue-shifted (365 nm) from that of $HTiNbO_5$ (387 nm or 3.2 eV), whereas $HTiNbO_5$/Fe-100 °C and $HTiNbO_5$/Fe-300 °C showed an absorption edge at 590 nm (2.1 eV) and 610 nm (2.03 eV), respectively. But the absorption in the visible-light region was highly diffuse. The difference in their absorption edge by incorporation of iron is due to the difference in band-gap energies of iron oxides and $HTiNbO_5$, and the composite material showed the combination of the two absorptions by $HTiNbO_5$ and the iron species. The synthesized samples of $HTiNbO_5$/Fe-100 °C and $HTiNbO_5$/Fe-300 °C were yellow, indicating the absorption of visible light, whereas the host material itself was white because it absorbed only UV light. A similar trend was observed for $HTiTaO_5$, $HTiTaO_5$/*n*-$C_3H_7NH_2$, $HTiTaO_5$/Fe-100 °C, and $HTiTaO_5$/Fe-300 °C, as shown in Fig. 3B. The band-gap energies measured by UV-DR are summarized in Table 1. The band-gap energies of iron-containing composite materials were the same at 2.0 eV, because they were determined by iron species regardless of the host material.

The morphologies of alkyl amine-intercalated (*n*-$C_3H_7NH_2$) layered compounds of $HTiNbO_5$ and $HTiTaO_5$ were examined by SEM as shown in Fig. 4. Both materials show bundles of stacked platelets (Figs. 4A and 4B). Each platelet showed fringes of a regular interval of ca. 20 nm, which was roughly consistent with the interlayer spacings of these materials measured by XRD. Each platelet appeared to be made of ca. 10 layers. SEM images of iron incorporated into the interlayer space of layered compounds (calcined at 300 °C) are shown in Figs. 4C and 4D. The spacing between platelets was expanded by the intercalated iron species between the layers of the host lattice. Although they still maintained a loose bundle, there was no regular stacking

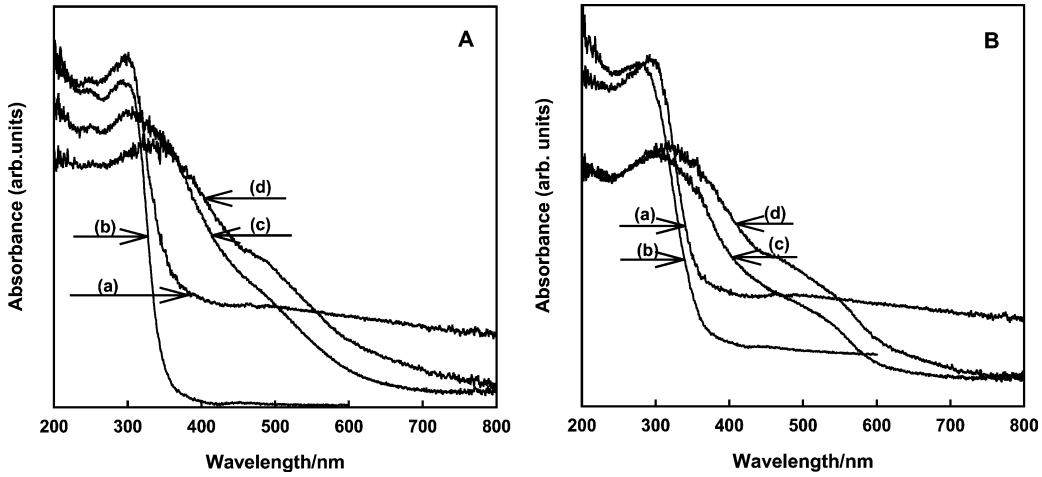

Fig. 3. A: UV-DR spectra of (a) $HTiNbO_5$, (b) $HTiNbO_5$/*n*-$C_3H_7NH_2$, (c) $HTiNbO_5$/Fe-100 °C, (d) $HTiNbO_5$/Fe-300 °C. B: UV-DR spectra of (a) $HTiTaO_5$, (b) $HTiTaO_5$/*n*-$C_3H_7NH_2$, (c) $HTiTaO_5$/Fe-100 °C, (d) $HTiTaO_5$/Fe-300 °C.

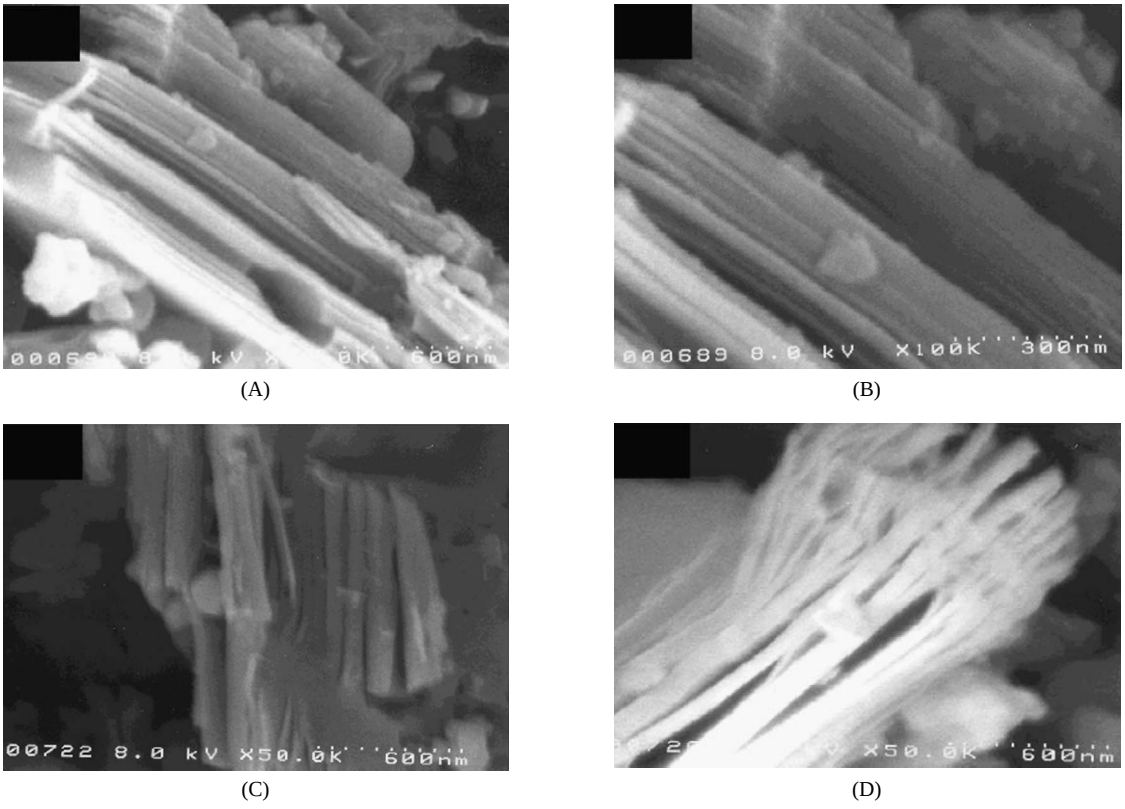

Fig. 4. SEM images of propylamine and iron intercalated into layered compounds (A) $HTiNbO_5$/*n*-$C_3H_7NH_2$, (B) $HTiNbO_5$/Fe, (C) $HTiTaO_5$/*n*-$C_3H_7NH_2$, (D) $HTiTaO_5$/Fe.

of platelets. The lateral sizes of platelets were also reduced. These observations explain the reduced (200) peak intensity of iron-intercalated samples in Fig. 2. The specific surface areas of iron-intercalated layered compounds were 4 times greater than those of host materials as shown in Table 1. This observation could be understood in terms of the above two factors: the expansion of platelet–platelet distances and reduced thickness of platelets upon intercalation of iron, exposing new surfaces between the platelets.

3.2. Electronic properties of intercalated iron species

To investigate the electronic and local coordination structures and oxidation state of iron oxide intercalated into the titania-niobate and titania-tantalate layers, the intercalated iron oxide was examined by XANES of the Fe K-edge. XANES represents electronic transition from an inner core level to the outer unoccupied levels caused by X-ray absorption, thus giving information on the local electronic

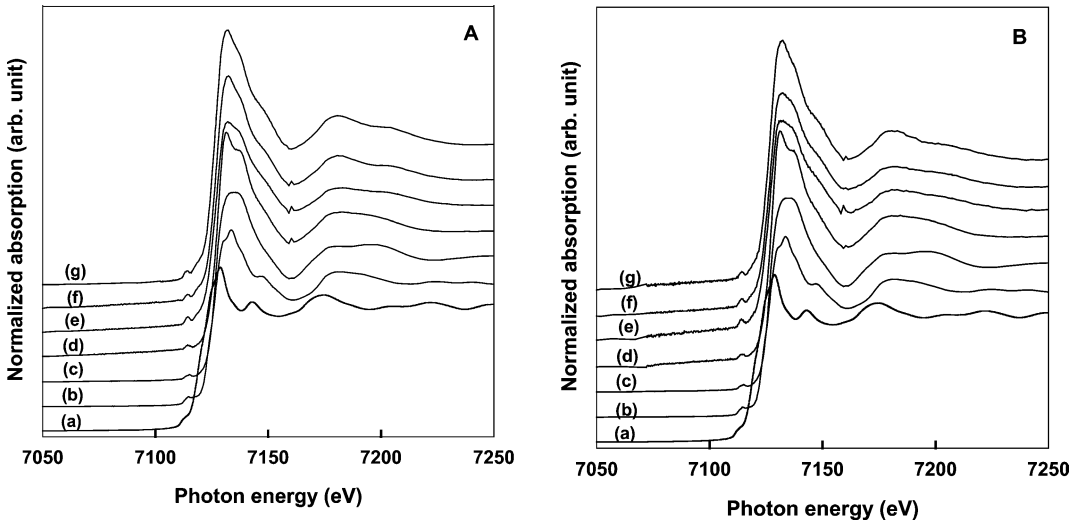

Fig. 5. A: Fe K-edge XANES spectra of (a) FeO, (b) Fe_2O_3 (c) Fe(III)-acetate precursor, (d) $HTiNbO_5$/Fe-100 °C, (e) $HTiNbO_5$/Fe-300 °C, (f) $HTiNbO_5$/Fe-400 °C, (g) $HTiNbO_5$/Fe-600 °C. B: Fe K-edge XANES spectra of (a) FeO, (b) Fe_2O_3, (c) Fe(III)-acetate precursor, (d) $HTiTaO_5$/Fe-100 °C, (e) $HTiTaO_5$/Fe-300 °C, (f) $HTiTaO_5$/Fe-400 °C, (g) $HTiTaO_5$/Fe-600 °C.

structure and coordination environment around an absorbing atom.

Fig. 5 shows the Fe K-edge XANES spectra for the iron-pillared derivatives of titania-niobate (A) and titania-tantalate (B) prepared at different calcination temperatures (d–g), compared with the reference samples, such as bulk FeO (a), Fe_2O_3 (b), and Fe-acetate precursor (c). The XANES spectra for Fe_2O_3 and the Fe(III)-acetate precursor exhibited weak pre-edge peaks at 7113.8 and 7115.2 eV, respectively, in the pre-edge region. This indicates that Fe^{3+} in these samples is located at a centrosymmetric octahedral site (*Oh*), and the 1s → 3d transition, an electric dipole-forbidden transition by parity consideration, has occurred. This result is in agreement with that of a previous work of Yamanaka et al. [18]. This pre-edge peak was not observed for FeO. When the Fe(III) acetate-precursor was intercalated into the interlayer spaces of titania-niobate and titania-tantalate layers (spectra d), the intercalated iron ion had a weak absorption peak in the pre-edge region. This result indicates that although the iron ions are intercalated into the layers, the iron still remains in an octahedral environment. When the intercalated iron derivatives were heated at 100–600 °C in air, the intercalated iron intermediate species were converted into iron oxides. It was observed that the iron oxide calcined at higher temperatures had the stronger absorption peak in the pre-edge region. This result suggests that the asymmetric electric potential forced by the negatively charged niobate layers leads to a noncentrosymmetric distortion of the FeO_6 octahedral structures, causing a stronger absorption peak in the pre-edge region. A noncentrosymmetric distortion would allow mixing of 3d and 4p orbitals, and an increase in the absorption intensity in the pre-edge region [19]. When all absorption features between the calcined samples (d–g) and the references samples (a–c) were compared, it could be concluded that the intercalated iron oxide had electronic and local coordination structures similar to those of Fe_2O_3 rather than FeO.

Table 2
Fe K-edge energies of the references and iron oxide samples intercalated into layered compoundperovskites material

	Sample names	Edge energy[a] (eV)
Reference	Fe foil	7112.1
	FeO(II)	7117.8
	Fe_3O_4(II and III)	7120.9
	Fe_2O_3(III)	7122.5
	Fe(III)-acetate precursor	7126.3
Intercalated samples	$HTiNb(Ta)O_5$/Fe-100 °C	7127.4 (7127.6)
	$HTiNb(Ta)O_5$/Fe-300 °C	7127.6 (7127.5)
	$HTiNb(Ta)O_5$/Fe-400 °C	7127.4 (7127.5)
	$HTiNb(Ta)O_5$/Fe-600 °C	7127.4 (7127.4)

[a] The numbers (eV) in parentheses are for tantalium derivatives of layered compounds.

The most prominent feature of XANES spectra for iron oxide intercalated between layers of layered compounds was the large white line areas of the main 1s → 4p transition. The white-line areas increased with calcination treatment temperature. The white-line area represents the extent of an empty orbital. Thus the intercalated iron oxide species appear to be in a highly electron-deficient state. These results are consistent with the Fe K-edge energies of Fe_2O_3 intercalated into the interlayer of layered compounds shown in Table 2. The edge energies for different samples are also listed in Table 2 for comparison. Iron oxide-intercalated layered compounds prepared under different calcination temperatures have X-ray absorption edges of higher energy than those of bulk Fe(II) and Fe(III). This feature has not been observed for unsupported nanosized Fe_2O_3 particles [20] and indicates that this effect originates not from the nanosize of

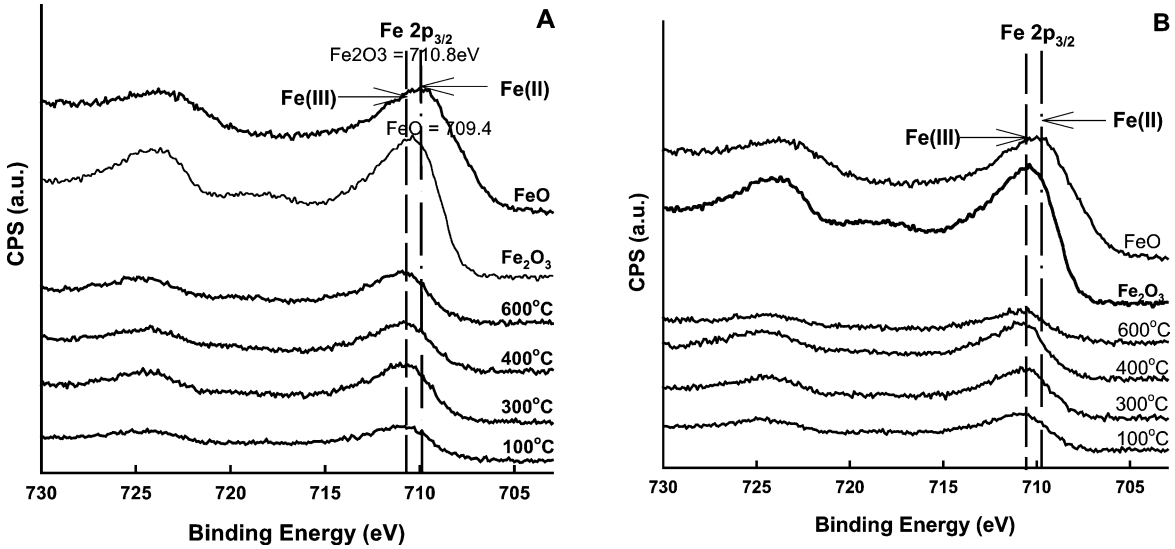

Fig. 6. A: XPS Fe $2p_{3/2}$ core-level spectra for (a) $HTiNbO_5$/Fe-100 °C, (b) $HTiNbO_5$/Fe-300 °C, (c) $HTiNbO_5$/Fe-400 °C, (d) $HTiNbO_5$/Fe-600 °C, (e) Fe_2O_3, (f) FeO. B: XPS Fe $2p_{3/2}$ core-level spectra for (a) $HTiTaO_5$/Fe-100 °C, (b) $HTiTaO_5$/Fe-300 °C, (c) $HTiTaO_5$/Fe-400 °C, (d) $HTiTaO_5$/Fe-600 °C, (e) Fe_2O_3, (f) FeO.

Fe_2O_3, but from the environment of Fe_2O_3 in the interlayer of layered compounds.

XPS measurements were carried out to investigate the oxidation state of iron intercalated in the layered structure. Fig. 6 shows the XPS Fe $2p_{3/2}$ core-level spectra for samples calcined at different temperatures together with reference samples of Fe_2O_3 and FeO. The XPS spectra for iron intercalated between the titania-niobate and titania-tantalate layers showed a large peak, assigned to trivalent iron at approximately 710.8 eV, which was almost the same as that of Fe_2O_3 rather than FeO (B.E. = 709.4 eV), and no other oxidation states were found. When the intercalated derivatives were heated from 100 to 600 °C, the intercalated iron precursor species was converted into Fe_2O_3. However, the binding energy of iron intercalated in the layers was not the same as that of the reference Fe_2O_3, but was shifted to a higher energy, because the iron intercalated between layers was a highly electron-deficient species relative to trivalent bulk iron. This result is consistent with Fe K-edge energies in Table 2 and white-line areas shown in Fig. 5 obtained from XANES spectra. The electron deficiency of intercalated Fe_2O_3 nanoparticles indicated by XANES and XPS, and apparent intensification of the XANES pre-edge peak by heating, could be taken as evidence that suggests a strong interaction between Fe_2O_3 nanoparticles and the host layered materials. The nanosize of Fe_2O_3 particles is not responsible for these observations, since bare Fe_2O_3 nanoparticles do not show such behavior [20].

3.3. Photocatalytic activity for water splitting

The photocatalytic activities of host and intercalated layered compounds were measured under UV and visible-light irradiation. As shown in Figs. 7 and 8, all of the catalysts showed photocatalytic activity for water splitting under UV irradiation ($\lambda > 200$ nm), and there was no indication of catalyst deactivation for 9 h, during which the catalyst turned over many times, making this overall water-splitting reaction "photocatalytic." The stoichiometric amounts of hydrogen and oxygen (2:1 by volume) were produced in all cases under UV. The amounts of gases evolved under UV light irradiation increased in the following sequence for $HTiNbO_5$ series: $HTiNbO_5$ (45 μmol/h for H_2, 22 μmol/h for O_2) > $KTiNbO_5$ (39 μmol/h for H_2, 19 μmol/h for O_2) > $HTiNbO_5/Fe_2O_3$ (15 μmol/h for H_2, 8 μmol/h for O_2). The difference between K^+-type and proton-type titanium niobate was very small. But intercalation of Fe_2O_3 reduced the H_2 production rate significantly. The reason for this detrimental effect of the intercalated Fe_2O_3 nanoparticles on the photocatalytic activity of the layered compounds under UV light is not clear. It is possible that the Fe_2O_3 nanoparticles played the role of recombination center. Alternatively, the absorption of UV light by Fe_2O_3 nanoparticles could also reduce the water-splitting rate by the layered compounds because Fe_2O_3 would not contribute to the hydrogen production as discussed below. A similar trend of hydrogen production was observed for $HTiTaO_5$ series, but there was a more significant difference between K^+-type and H^+-type layered materials.

Fig. 7 also shows the rate of H_2 evolution from water in the presence of a sacrificial hole acceptor (CH_3OH) under visible-light irradiation ($\lambda > 420$ nm). Hydrogen was produced only during the first run and only during the initial period (< 1 h) of the first run. After evacuation, there was no hydrogen production from the second run. Similar results were observed for iron oxide intercalated in $HTiTaO_5$. Thus, unlike in the previous report [14], Fe_2O_3 nanoparticles do not produce hydrogen in a photocatalytic manner under visible light. Wu et al. [14] reported that the intercalated Fe_2O_3 showed photocatalytic activity of H_2 evolution from

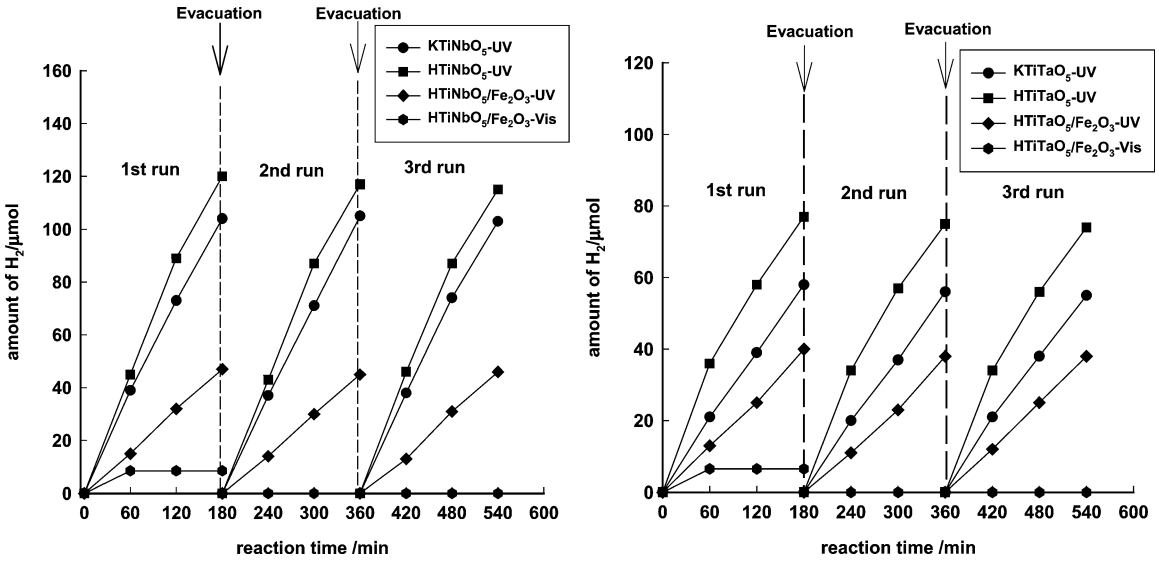

Fig. 7. Amount of H_2 evolution according to reaction time of host and intercalated layered compounds under UV and visible light irradiation. (Left) Titanium niobate based catalysts. (Right) Titanium tantalite based catalysts. UV reactions; 0.3 g catalysts, 500 ml pure water, 450 W Hg lamp. Visible light reactions; 0.1 g catalysts, 80 ml H_2O + 20 ml CH_3OH, 500 W Hg lamp with a cutoff filter (> 420 nm).

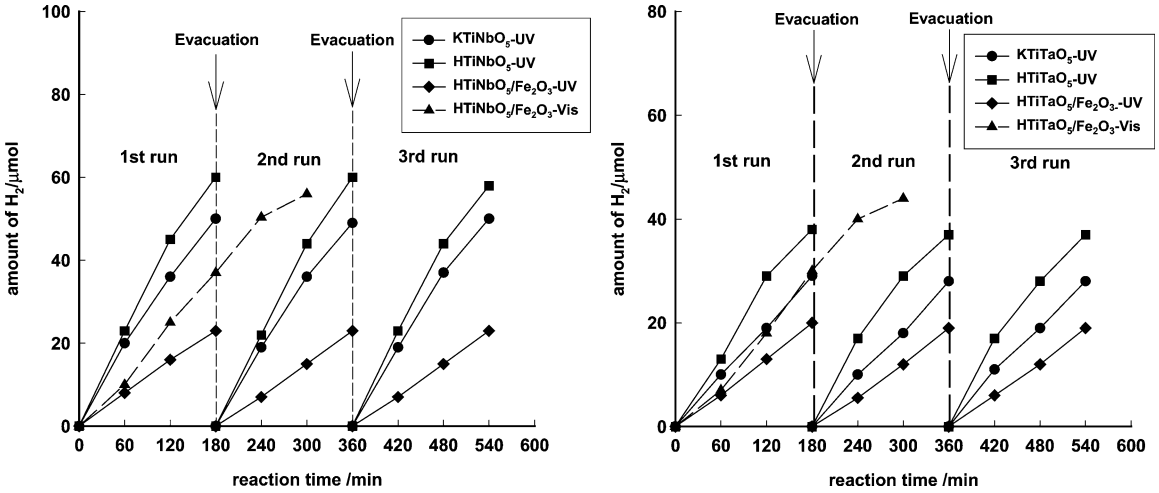

Fig. 8. Amount of O_2 evolution according to reaction time of host and intercalated layered compounds under UV and visible light irradiation. (Left) Titanium niobate based catalysts. (Right) Titanium tantalite based catalysts. UV reactions; 0.3 g catalysts, 500 ml pure water, 450 W Hg lamp. Visible light reactions; 0.1 g catalysts, 0.0l M $AgNO_3$ 100 ml aqueous solution, 500 W Hg lamp with a cutoff filter (> 420 nm).

a CH_3OH–H_2O solution by transfer of the photoelectron from Fe_2O_3 to the host layered compound, which decreased the recombination of electrons and holes under visible-light irradiation. However, it was found in this work that hydrogen evolution under visible light was not due to photocatalytic decomposition of water. On the other hand, as shown in Fig. 8, O_2 evolution in the presence of an electron acceptor ($AgNO_3$) under visible-light irradiation ($\lambda > 420$ nm) increased steadily for 5 h with a rate as high as those under UV light.

This lack of photocatalytic activity under visible light could be rationalized by considering the band structure of the material as shown schematically in Fig. 9. Thus, layered compound $HTiNb(Ta)O_5$ is a UV-active photocatalyst of overall water splitting that produces H_2 and O_2 simultaneously because the conduction bands are located at a more negative position than the reduction potential of H^+ to H_2, whereas the valence band positions are more positive than the oxidation potential of OH^- to O_2 (Fig. 9a). However, it does not absorb visible light because of the large band-gap energy. When Fe_2O_3 nanoparticles are intercalated into the interlayers of the layered compounds, the obtained composite material now absorbs visible light due to Fe_2O_3, but cannot produce hydrogen because the conduction band bottom of Fe_2O_3 is located at a less negative position than the reduction potential of H^+ to H_2 (Fig. 9b). The small amount of hydrogen produced initially may be from the charge-balancing proton between the interlayer of layered compounds. It should be noted that the host materials studied by Wu et al. [14] contained tungsten instead

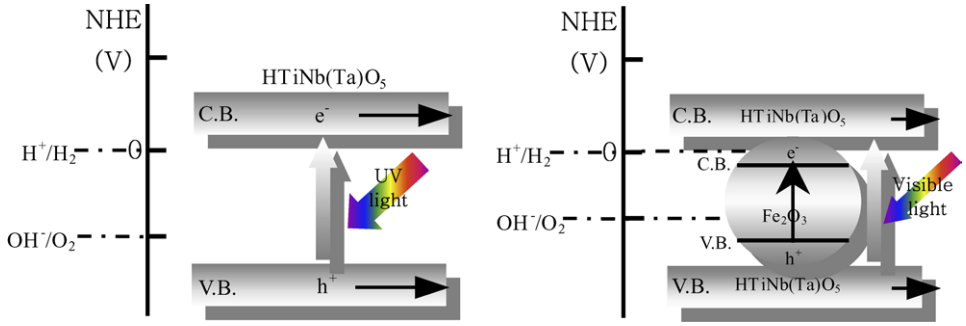

Fig. 9. An electronic band structures and generation of electrons and holes; (a) $HTiNb(Ta)O_5$ has proper band positions for both water reduction and oxidation, but absorbs only UV light due to large-band gap energy. (b) Fe_2O_3–$HTiNb(Ta)O_5$ absorbs visible light, but the conduction band position of Fe_2O_3 is not negative enough to reduce water.

of titanium included in the materials studied here. Yet they have the same structure and thus it is believed that the conclusions obtained here could be applied to their materials as well. On the other hand, the materials produced oxygen in a photocatalytic manner, as expected from the position of valence band top of iron oxide intercalated into layered compounds, which is located at a more positive position than the oxidation potential of OH^- to O_2. In any case, iron oxide intercalated in layered compounds is a good visible light-active photocatalyst for oxygen production from water, but it is not a hydrogen-producing photocatalyst under visible light.

One interesting characteristic of the nanosized Fe_2O_3 particles intercalated into the compound layers was their high electron deficiency relative to bulk Fe_2O_3. The electron deficiency suggests a strong electronic interaction between the nanoparticles and the host layers. This interaction could work favorably for photocatalysis because of an efficient electron–hole separation. Indeed, O_2 evolution in the presence of an electron acceptor ($AgNO_3$) under visible light proceeded at a high rate comparable to those under UV light. A direct comparison of the reaction rates under visible light and UV light is meaningless because of the presence and absence of the sacrificial agent in water, respectively. Yet, it is significant that the catalyst showed comparable O_2 evolution rates under both UV and visible light. This may prove the validity of the concept of intercalation of an active photocatalyst into a layered compound to create an active composite photocatalyst. This concept could be further exploited to devise an efficient hydrogen-producing, visible-light photocatalyst by the intercalation of other semiconductors with proper band positions, such as CdS [12].

4. Conclusions

Nanosized Fe_2O_3 particles were intercalated into the interlayer space of $HTiNbO_5$ and $HTiTaO_5$ by successive intercalation reactions. The presence of Fe_2O_3 in the interlayer space of a layered compound induced the absorption of visible light that was absent for host layered compounds. The iron oxide intercalated into the interlayer space of $HTiNbO_5$ or $HTiTaO_5$ has electronic and crystal structures similar to those of Fe_2O_3, but it is in a highly electron deficient state. Unlike in a previous report, however, Fe_2O_3-intercalated layered compounds did not lead to photocatalytic H_2 production from water reduction under visible-light irradiation. Yet it showed a high activity for oxygen production from water oxidation.

Acknowledgments

This work was supported by the General Motors R&D Center, the Hydrogen Energy R&D Center, one of the 21st Century Frontier R&D Programs, the Brain Korea 21 Project, the National R&D Project for NanoScience and Technology, and the Research Center for Energy Conversion and Storage through KOSEF.

References

[1] A. Fujishima, K. Honda, Nature 238 (1972) 37.
[2] J. Kim, D.W. Hwang, H.G. Kim, S.W. Bae, J.S. Lee, L. Wei, S.H. Oh, Top. Catal., in press.
[3] H. Kato, K. Asakura, A. Kudo, J. Am. Chem. Soc. 125 (10) (2003) 3082.
[4] K. Domen, M. Hara, J.N. Kondo, T. Takata, A. Kudo, H. Kobayashi, Y. Inoue, Korean J. Chem. Eng. 18 (5) (2001) 862.
[5] G. Hitoki, H. Takata, J.N. Kondo, M. Hara, H. Kobayashi, K. Domen, Electrochem. 70 (6) (2002) 463.
[6] A. Kudo, M. Sekizawa, Chem. Commum. (2000) 1371.
[7] R. Abe, K. Sayama, K. Domen, H. Arakawa, Chem. Phys. Lett. 344 (2001) 339.
[8] Z. Zou, J. Ye, K. Sayama, H. Arakawa, Nature 414 (6) (2001) 625.
[9] R. Abe, H. Hara, K. Sayama, K. Domen, H. Arakawa, J. Photochem. Photobiol. A: Chem. 137 (2000) 63.
[10] A. Kasahara, K. Nukumizu, T. Takata, J.N. Kondo, M. Hara, H. Kobayashi, K. Domen, J. Phys. Chem. B 107 (2003) 791.
[11] W. Shangguan, A. Yoshida, J. Phys. Chem. B 106 (2002) 12227.
[12] J. Wu, J. Lin, S. Yin, T. Sato, J. Mater. Chem. 11 (2001) 3343.
[13] J. Wu, S. Uchida, Y. Fujishiro, S. Yin, T. Sato, Int. J. Inorg. Mater. 1 (1999) 253.
[14] J. Wu, S. Uchida, Y. Fujishiro, S. Yin, T. Sato, J. Photochem. Photobiol. A: Chem. 128 (1999) 129.
[15] Y. Chung, S.K. Lim, C.K. Kim, Y. Kim, C.S. Yoon, J. Magn. Magn. Mater. 272 (2004) E1167.

[16] L.H. Huo, X.L. Li, W. Li, S.Q. Xi, Sens. Actuat. B: Chem. H 71 (1–2) (2000) 77.
[17] P. Li, D.E. Miser, S. Rabiei, R.T. Yadav, M.R. Hajaligol, Appl. Catal. B 43 (2) (2003) 151.
[18] S. Yamanaka, M. Hattori, Catal. Today 2 (1988) 261–270.
[19] Y. Han, S. Choi, J. Jang, D. Kim, J. Solid State Chem. 160 (2001) 435.
[20] L.X. Chen, T. Liu, M.C. Thurnauer, R. Csencsits, T. Rajh, J. Phys. Chem. B 106 (2002) 8539–8546.